Materials Research Express

PAPER

# An experimental and theoretical study on nanomachining forces along zigzag and armchair lattice orientations of monolayer $MoS_2$

**Meng Li**[1,2,6], **Yu Zhang**[3], **Lu Wang**[4], **Ning Xi**[5], **Xiaoning Xin**[1], **Xiaoshi Jin**[1] and **Meile Wu**[1,6]

[1] College of Information Science and Engineering, Shenyang University of Technology, Shenyang, People's Republic of China
[2] State Key Laboratory of Robotics, Shenyang Institute of Automation, Chinese Academy of Sciences, Shenyang, People's Republic of China
[3] Department of Computer Science and Technology, Changchun Normal University, Changchun, People's Republic of China
[4] Liaoning equipment manufacturing Vocational and Technical College, Shenyang 110161, People's Republic of China
[5] Department of Industrial & Manufacturing Systems Engineering, University of Hong Kong, Pokfulam, Hong Kong Special Administrative Region of the People's Republic of China
[6] Authors to whom any correspondence should be addressed.

**E-mail:** limeng_sut@163.com **and** meil.w@hotmail.com

**Keywords:** AFM, nanofabrication, $MoS_2$, zigzag and armchair

Supplementary material for this article is available online

OPEN ACCESS

RECEIVED
3 July 2020

REVISED
19 August 2020

ACCEPTED FOR PUBLICATION
27 August 2020

PUBLISHED
4 September 2020



## Abstract

Recent progresses in the synthesis of large-area and stable atomically thin $MoS_2$ have evoked enormous interest toward the future applications of two-dimensional (2D) electronics. Although considerable theoretical researches have been conducted to examine the zigzag and armchair lattice orientations of $MoS_2$, which are closely related to the physical and chemical properties of this material, experimental investigations into these two orientations are still quite rare. In this paper, we present an experimental study on nanofabrication along the zigzag and armchair orientations of monolayer $MoS_2$ using normal- and phase-mode AFM. After identifying the zigzag and armchair orientations, distinctly different nanofabrication forces along these two orientations are obtained, which are approximately 15.9 nN and 35.8 nN, respectively. To determine the underlying mechanism of this discrepancy, molecular dynamics simulation is performed. The simulated nanofabrication forces along the zigzag and armchair orientations are $12.16 \pm 0.59$ nN and $21.45 \pm 0.74$ nN, respectively, in good agreement with the experimentally measured ones. The results provide a better understanding of the zigzag and armchair lattice orientations of monolayer $MoS_2$ as well as a promising approach to closed-loop fabrication of 2D materials with desirable lattice orientations.

## 1. Introduction

The successful isolation and characterization of graphene has helped usher in the era of two-dimensional (2D) layered materials and provided new perspectives for the fabrication of electronic/optoelectronic devices from such materials [1–3]. Although graphene has been widely studied owing to its clear advantages, its application in device fabrication is still greatly hindered by the absence of an intrinsic band gap [4, 5]. As a result, researchers have been striving to search for alternative 2D materials. TMDCs, a large family of 2D materials with a wide range of electronic, optical, mechanical properties that are complementary to yet distinctive from those of graphene, have met with wild enthusiasm from the research community [6–10]. One of most popular ones is $MoS_2$, which is characterized by bandgap variability, reasonably high carrier mobility, as well as remarkable transparency, flexibility and stability [11–13]. Meanwhile, $MoS_2$-based electronic and optoelectronic nanodevices have been fabricated and widely used in many relevant fields [14–17], which demonstrates the enormous potential of $MoS_2$.

Most $MoS_2$-based nanodevices today are fabricated by pristine $MoS_2$, which means that the properties or the appearance of $MoS_2$ remain unchanged during the fabrication process. Given that sophisticated structures with tailored properties and well-defined geometries are crucial for real-world applications of $MoS_2$, the focus of

many studies has been shifted to the edge engineering of $MoS_2$. This approach can achieve both tunable properties and customized parameters, such as size or shape. It is well known that zigzag and armchair lattice orientations are highly sensitive to the termination of the $MoS_2$ structure and thus play a significant role in determining the physical and chemical properties of $MoS_2$ [18–21]. Theoretical analysis has shown that $MoS_2$ has ferromagnetic metallic zigzag edges and nonmagnetic semiconducting armchair edges. Due to this fundamental discrepancy, zigzag $MoS_2$ nanoribbons exhibit enhanced properties in terms of Li atom adsorption, valley polarized current and resonant electronic transport [22], and can serve as promising cathode materials [23] and piezoelectronics [24]. The armchair $MoS_2$ edges, however, have semiconducting and tunable bandgap characteristics [25], which makes them more suitable for fabricating ultra-narrow electronic devices [26, 27].

Although considerable theoretical guidance has been provided to underscore the importance of edge engineering, direct observation and fabrication of these two types of edges have been quite rare and extremely difficult. In most cases, high-resolution transmission electron microscopy (TEM) is used to observe the sample surface and obtain the complete lattice orientation distribution. Nevertheless, it can be difficult to use TEM to achieve high-quality lattice imaging and distinguish the distinct zigzag or armchair edges of $MoS_2$. This is because this approach involves a time-consuming and costly pre-processing process that typically requires complex sample preparation and careful execution. What's worse, TEM has an internal construction and an operation mechanism that limit its use in 2D material fabrication to a few nanometers or even the atomic scale [28]. This in turn makes it impossible to meet the real-world industrial needs for large-scale edge engineering of 2D materials. Given the insufficient knowledge of these two special edges and the shortcomings of TEM, it is imperative to experimentally investigate these two lattice orientations so as to develop a convenient and cost-free fabrication method.

In this study, we examined the zigzag and armchair orientations of monolayer $MoS_2$ by nanomachining along the identified lattice orientations. First, we performed nanomachining along these two types of edges by normal-mode AFM. Then we measured and compared the nanomachining forces along the zigzag and armchair orientations of monolayer $MoS_2$ when different loads were applied. To overcome the disadvantages of normal-mode AFM fabrication, we used ultrasonic vibration-assisted AFM instead to perform phase-mode nanomachining to determine the appropriate load force for monolayer $MoS_2$. With this load force, the accurate nanomachining force values along the zigzag and armchair orientations of monolayer $MoS_2$ were obtained, which were 15.9 nN and 35.8 nN, respectively. To better understand the underlying mechanism of nanofabrication, theoretical calculation and corresponding analysis were performed. The molecular dynamics (MD) simulated nanomachining forces along the zigzag and armchair orientations were approximately $12.16 \pm 0.59$ nN and $21.45 \pm 0.74$ nN, respectively, which agreed well with the experimental measured values. The significant nanomachining force discrepancy between the zigzag and armchair orientations will serve as a key component to establishing a close-loop AFM edge engineering strategy with controllable lattice orientations.

## 2. Material and methods

### 2.1. Sample preparation and characterization

The monolayer $MoS_2$ nanosheets, which were purchased from Six Carbon, Shenzhen, China, were synthesized by chemical vapor deposition (CVD) and deposited on a square (1 cm wide) piece of P-doped Si wafer with a 300 nm oxide layer. To ensure the surface was clean and flat enough to facilitate the subsequent lattice orientation identification and nanomachining, the surface morphology of the sample was characterized by AFM (Icon, Bruker). The measurements (figure 1(a)) show that the sample had a height of around 0.75 nm. Considering the ultra-low thickness and the possible measurement error, Raman spectroscopy, a reliable and powerful technique to determine the layer numbers of 2D materials [29], was also used to accurately estimate the thickness of the sample. The Raman spectrum for $MoS_2$ (figure S1 is available online at stacks.iop.org/MRX/7/095002/mmedia) agrees well with that reported in literature [30] and indicates the sample was a monolayer $MoS_2$ nanosheet.

According to [31], for the CVD monolayer $MoS_2$ nanosheet in the shape of a triangle, the direction of the hypotenuse is typically identified as the zigzag orientation due to the energetic stability, and the direction perpendicular to the hypotenuse is identified as the armchair orientation. Notably, the zigzag and armchair orientations, instead of the precise edge termination or the atomic structure, are defined as microscale orientations, which is because the nano-scale edge can be rough and unpredictable based on the results observed from TEM [31]. To guarantee the consistency between the nanomachining direction and the target lattice orientation without adding complexity to the experiment, we also employed the single-line-scan power spectrum analysis technique proposed in one of our previous works [32]. This technique can detect the lattice orientation from the friction measurements and frequency characteristics of the tested regions in a simple and

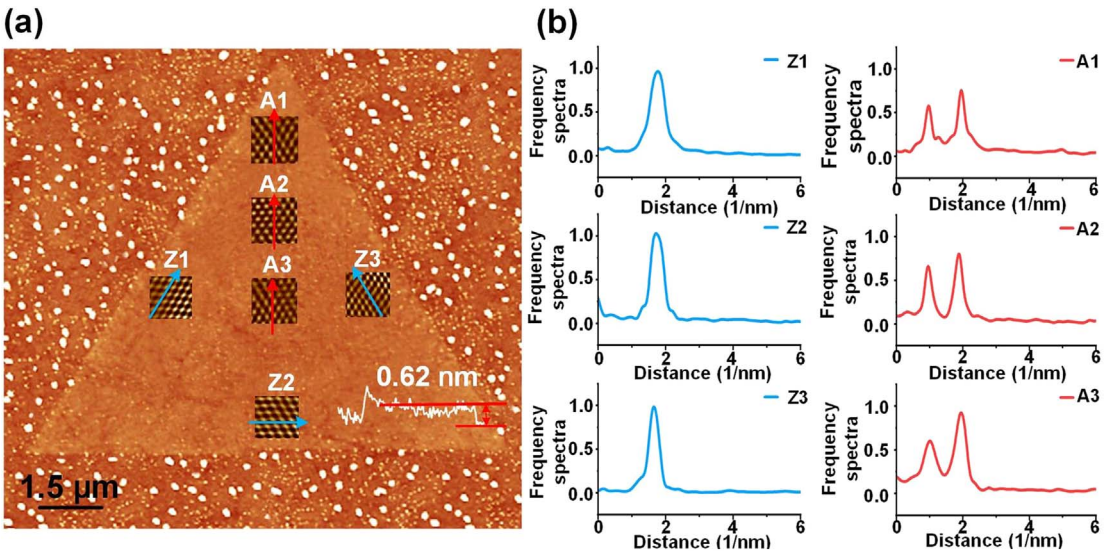


**Figure 1.** AFM imaging and frequency characteristics of the CVD-grown $MoS_2$ nanosheet. (a) is the AFM image of the $MoS_2$ nanosheet and contains the atomic images obtained from the randomly chosen regions on the $MoS_2$ nanosheet along the zigzag and armchair orientations and labeled as Z1, Z2, and Z3, and A1, A2, and A3, respectively. The blue and red arrows indicate the zigzag and armchair orientations. (b) shows the frequency spectra of the friction signals obtained from the regions of Z1, Z2, and Z3, and A1, A2, and A3.

low-cost way. The necessary tribological information can be obtained from lateral friction microscopy (LFM) by using the contact mode of multimode scanning probe microscopy (SPM) in the air and under ambient conditions (MLCT, Burker, relative humidity: 43 to 47%; temperature: 20 to 40 °C). During the scanning process, a normal contact silicon nitride probe with a 0.02 N $m^{-1}$ spring contact was used to deliver a scan size of 10 × 10 nm and a scan rate of 29.5 Hz. Following the detection process by the single-line-scan power spectrum analysis technique, several regions along the two nanomachining directions were randomly chosen and LFM was performed within the target regions. After 5–10 s of operation, atomic images with a low atomic resolution were obtained, which were labeled as Z1, Z2, and Z3, and A1, A2, and A3, respectively. Then the friction signal and the corresponding frequency characteristics along the direction parallel or perpendicular to the hypotenuse of the $MoS_2$ nanosheet could be extracted through FFT calculation. As shown in the frequency spectra (figure 1(b)), the frequency characteristics along the two nanomachining directions were consistent with those along the zigzag and armchair lattice orientations (only one and two frequency peaks). In this way, the two nanomachining directions should be consistent with zigzag and armchair orientations, and the microscale fabricated edges can also be reasonably identified as zigzag and armchair edges.

### 2.2. Nanomachining with normal- and phase-mode AFM

The nanomachining experiment was carried out by normal- and phase-mode AFM, respectively. The fabrication probe was made of diamond coated silicon nitride (DDESP, Bruker) with a radius of 150 nm and a normal spring constant of 42 N $m^{-1}$. The asymmetric structure of the diamond AFM probe will inevitably affect the nanomachining results when the fabrication direction is changed. Therefore, the fabrication direction of the AFM tip was kept unchanged and nanomachining along the zigzag and armchair orientations was achieved by rotating the substrate. For normal-mode AFM, nanomachining was realized with the aid of Icon-based manipulation software, which allows adjusting fabrication parameters such as deflection setpoint, cutting length, direction, and shape. Meanwhile, the PSD (position sensitive detector) signal could be automatically collected during the fabrication process for analyzing the fabrication results. The fabrication width was largely dependent on the tip radius, the tip broadening effect, and the degree of wear. Ultrasonic vibration-assisted AFM was established by adding a phase control module (Zurich Instruments AG, HF2LI) to the normal-mode AFM system. The experiment setup and underlying mechanism of normal- and phase-mode ultrasonic vibration-assisted AFM are shown in figures 2(a) and (b), which clearly shows the essential differences between these two fabrication methods. A more detailed description of the phase-mode AFM can be found in one of our previous works [33].

### 2.3. Nanomachining with normal- and phase-mode AFM

According to literature [34], a monolayer $MoS_2$ nanosheet can be regarded as a sandwich-like slab in which a Mo layer lies between the two S layers, and two individual atoms, Mo and S atoms, are covalently bonded with each

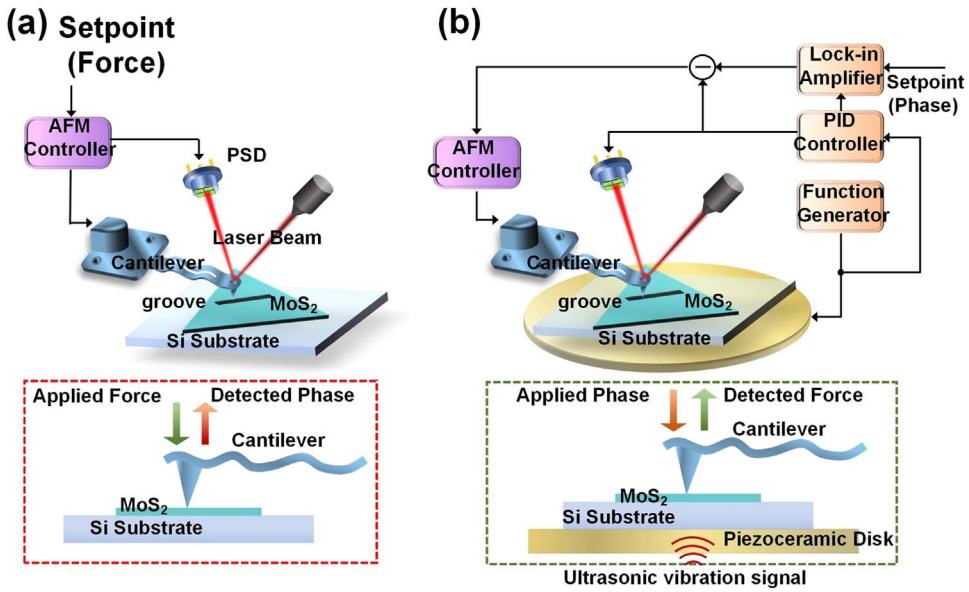


**Figure 2.** Schematic of normal- and phase-mode of AFM mechanical nanomachining. (a) shows the experiment setup of normal-mode AFM mechanical nanomachining, the underlying mechanism of which is marked in a red-dotted rectangle. (b) shows the experiment setup of phase-mode AFM mechanical nanomachining, the underlying mechanism of which is marked in a green-dotted rectangle.

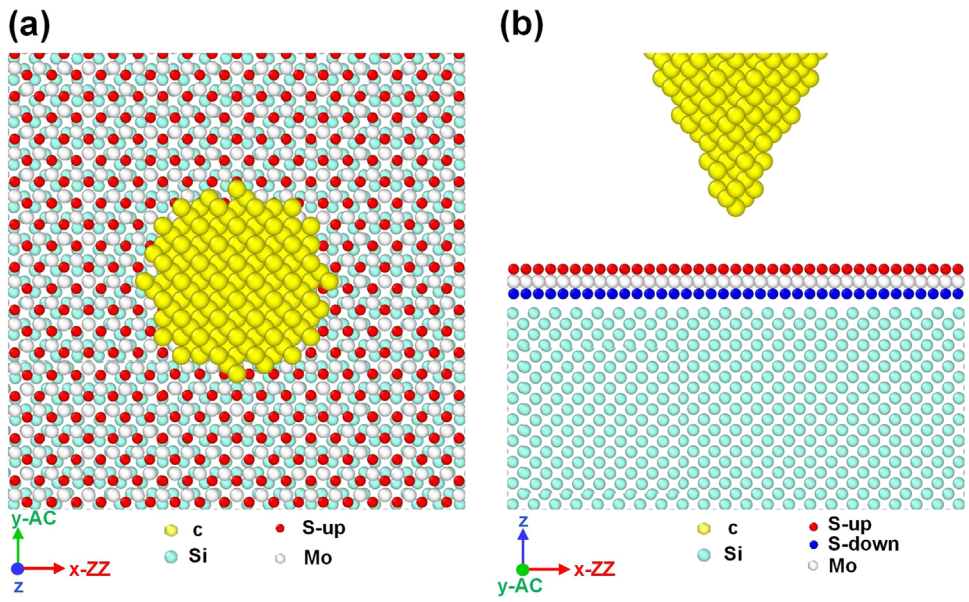


**Figure 3.** Computation model. (a) offers a top view of the 25 nm × 21 nm cell of the monolayer $MoS_2$ on the Si substrate with a diamond probe applied. (b) offers a lateral view of the initial state of the simulation process. The carbon, silicon, sulphur, and molybdenum atoms were labeled as (c), Si, S-up, S-down, and Mo, respectively.

other a lattice constant of 3.16 Å. With the above necessary elements available, the initial model of a 25 nm × 21 nm monolayer $MoS_2$ nanosheet that takes into account the interaction between the probe and Si substrate could be established, as shown in figure 3(a) (top view) and 3(b) (lateral view). Then, the open-source software—large-scale atomic/molecular massively parallel simulator (LAMMPS)—was used for molecular dynamics (MD) simulation. Moreover, a new Stillinger–Webber (SW) potential originating from the valence force-field model was used to describe the bond breaking, bond reforming, and the interatomic interactions of monolayer $MoS_2$ based on the pre-built-in accurate equilibrium structure information provided by SW potential [35, 36]. To mimic the AFM nanomachining process, a diamond probe (considering the AFM probe is coated with diamond) was applied on the monolayer $MoS_2$ nanosheet. For ease of simulation, the interaction between the internal C atoms of the diamond probe was ignored. For the probe-sample interaction, the one

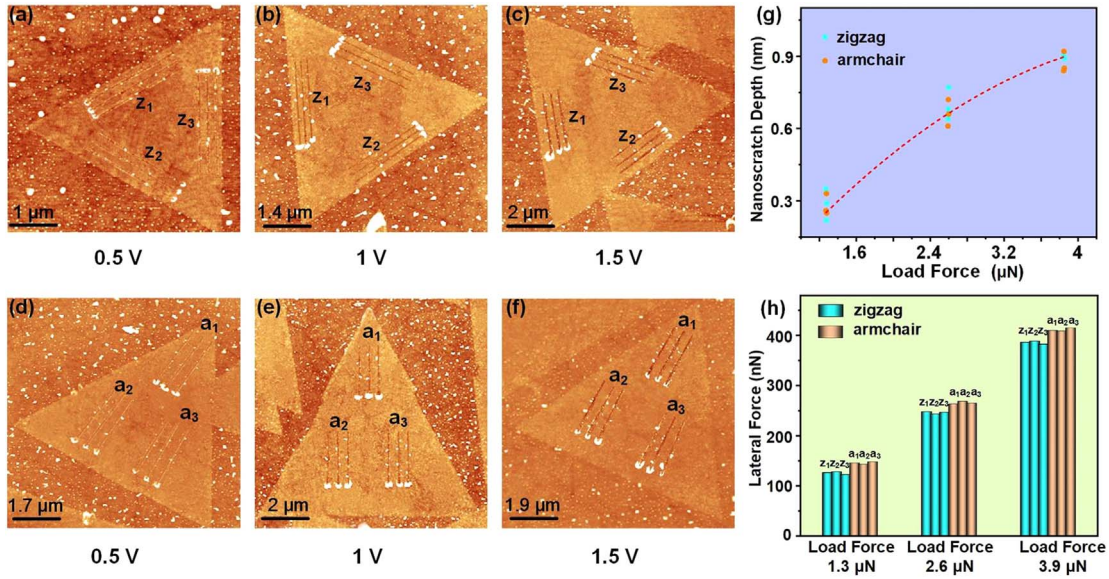


**Figure 4.** Results of normal-mode AFM nanofabrication on monolayer $MoS_2$. (a) to (c) are the results of fabrication along the zigzag orientation. Three fabrication regions were randomly chosen on each monolayer $MoS_2$ nanosheet, which were labeled as $z_1$, $z_2$, and $z_3$. (d) to (f) are the results of fabrication along the armchair orientation. Three fabrication regions were randomly chosen on each monolayer $MoS_2$ nanosheet, which were labeled as $a_1$, $a_2$, and $a_3$. (g) shows the depth measurements of the nanoscratches along the zigzag and armchair orientations. (h) shows the comparison of lateral forces when different load forces were applied.

between C-Mo and C-S atoms, however, Morse interaction was adopted with the parameters $=$ 0.087 eV, $a$ $=$ 5.14 Å$^{-1}$, and $r_0$ $=$ 2.05 Å. Furthermore, the interaction between the monolayer $MoS_2$ and the substrate was simulated by using the reduced LJ potential energy interaction as the limiting force. An LJ-type action wall was added at −3.25 Å below the Z axis of the Mo atom. In the form of LJ1043, the parameters were set as epsilon $=$ 0.012 eV, sigma $=$ 3.27 Å, and cutoff $=$ 7.7 Å.

## 3. Results and discussion

Considering the ultra-low thickness of the monolayer $MoS_2$, nanomachining was performed by applying a steadily increasing load force within the estimated range obtained based on past fabrication experience. To eliminate the influence of probe wear, we adopted the same AFM probe for each nanomachining experiment with a certain force applied. Moreover, the nanomachining speed was kept constant at 1 $\mu$m s$^{-1}$, which, as demonstrated by empirical experience, is appropriate for fabrication on $MoS_2$ nanosheets; the moving direction of the AFM probe was kept at an angle of 90° during machining. The fabrication was performed along the direction that is parallel or perpendicular to the hypotenuse and identified as zigzag or armchair lattice direction, and three fabrication regions were randomly chosen, which were labeled as $z_1$, $z_2$, and $z_3$ or $a_1$, $a_2$, and $a_3$. Within the fabrication regions, three nanoscratches with a cutting length of around 2.5 $\mu$m were obtained. The fabrication results are shown in figure 4. According to the AFM cantilever elastic model described in Supplementary Information, the three-dimensional nanomachining forces $F_x$, $F_y$, $F_z$ for each group were calculated using the following equation.

$$\begin{aligned} F_y &= k_l S_l V_l \\ F_x &= -F_y \cot \varphi \\ F_z &= kS_n V_n - \frac{h}{l} F_x \end{aligned} \tag{1}$$

where $S_l$ and $S_n$ are the lateral and vertical sensitivities of the AFM cantilever, $V_l$ and $V_n$ are the corresponding PSD voltage output signals, $k_l$ is the horizontal torque of the cantilever, $\varphi$ is the angle between the AFM probe moving direction and x-axis, and $k$ is the spring constant of the AFM probe. According to literature [37], the relationship between $S_l$ and $S_n$ can be described as $S_l = \frac{3}{2l} S_n$, and the accurate value of $S_n$ can be obtained from the slope of the force curve. $k_l$ can be further expressed as $k_l = \frac{Gwt^3}{3l(h + t/2)}$, where $G$ is the shear modulus of the cantilever, and $w$, $t$, $l$, and $h$ are the effective width, thickness, length and height of the AFM probe. The value of $G$ is approximately 0.5 $\times$ 10$^{11}$ Nm$^{-2}$, and the parameters of the AFM probe can be obtained from the measurement results in the scanning electron microscopy image (figure S2).

According to equation (1), for the AFM probe with a 90° angle, $F_x$ can be calculated as zero. The fabrication depth is mainly determined by the load force , and larger $F_z$ values will lead to deeper grooves on the sample surface. When a certain load force $F_z$ is applied, the lateral force $F_y$ will be the main cause of nanomachining along a specific direction, which consists of two parts: the real cutting force along the specific lattice orientation $F_c$, and the friction force between the AFM probe and the substrate $F_{friction}$. For normal-mode AFM nanomachining, it is extremely difficult to determine the accurate load force that is appropriate for fabrication on the ultra-thin monolayer $MoS_2$. Then, three groups of experiments were conducted using a varying load force $F_z$ and parameters selected based on past fabrication experience. As shown in figures 4(a) to (f), 0.5 V, 1 V, and 1.5 V were chosen as the $V_n$ values for comparison, and the corresponding $F_z$ values were calculated to be 1.3 $\mu$N, 2.6 $\mu$N, and 3.9 $\mu$N, respectively. Then the cutting depth and width of each nanoscratch were measured. The measurements showed that nanoscratches along the zigzag orientation generally had a smaller width than those along the armchair orientation (figure S3). The underlying mechanism will be discussed in the theoretical analysis section. Apart from the variation in width, the variation in the cutting depth of nano scratches increased monotonically with the load force, as shown in figure 4(g). Based on the cutting depth measurement and the thickness of the monolayer $MoS_2$ nanosheet, under- and over-cutting occurs for nanomachining with load forces of 1.3 $\mu$N and 3.9 $\mu$N, respectively. As a result, the $F_{friction}$ value determined by the interaction between the AFM probe and the substrate varies largely with different nanomachining cases. But fortunately, $F_{friction}$ barely changes when the same load force $F_z$ is applied and is not affected by the fabrication direction, then the difference in the cutting force $F_c$ between the zigzag and armchair orientations can still be obtained by comparing the values of lateral force $F_y$. Based on equation (1), the values of the varying lateral force $F_y$ along the zigzag and armchair orientations for each group were obtained and the comparisons are illustrated in figure 4(h). More detailed data are summarized in table S1. The comparisons show that the absolute values of $F_y$ vary little for nanoscratches in the same direction, but more significantly for those in different directions. For example, for the group with a load force of 2.6 $\mu$N, the lateral force values of the $z_1$, $z_2$, and $z_3$ regions can be obtained from the average values of the three nanoscratches for each region (248.2 nN, 243.5 nN, and 246.8 nN), and the biggest difference among them was merely 4.7 nN. Similarly, the lateral force values of the $a_1$, $a_2$, and $a_3$ regions were calculated to be 263.7 nN, 268.9 nN, and 265.2 nN, and the biggest difference among them was also very small (5.2 nN). By averaging the values of the $z_1$, $z_2$, and $z_3$, and $a_1$, $a_2$, and $a_3$ regions, the nanomachining force along the zigzag orientation $F_y(\bar{Z})$ and that along the armchair orientation $F_y(\bar{A})$ with a load force of 2.6 $\mu$N were calculated to be 246.2 nN and 265.9 nN, respectively, representing an evident difference (19.7 nN). This phenomenon was also observed for the other two fabrication groups with load forces of 1.3 $\mu$N and 3.9 $\mu$N, which can eliminate the possible interference by experimental measurement errors. The nanomachining force difference between the zigzag and armchair orientations was 20.7 nN with a load force of 1.3 $\mu$N and 25.5 nN with a load force of 3.9 $\mu$N. Considering the $F_{friction}$ value remains unchanged for the same group, the significant difference between $F_y(\bar{Z})$ and $F_y(\bar{A})$ can be reasonably attributed to the variation in the real cutting force $F_c$ along the zigzag and armchair orientations.

To calculate the accurate value of $F_c$, we should obtain the value of $F_{friction}$ first. Although this value cannot be directly extracted from nanomachining on $MoS_2$, it can be roughly evaluated from the fabrication on the adjacent substrate applied with the same load force $F_z$ as the nanomachining on the monolayer $MoS_2$ nanosheet. Notably, nanomachining with this load force $F_z$ should, as soon as it starts, accurately cut through the monolayer $MoS_2$ nanosheet without over- or under-cutting. This is to ensure that the AFM probe slides smoothly between the sample and the substrate and no extra force and energy are consumed on cutting the substrate during the fabrication process. However, normal-mode AFM can hardly achieve such high-precision fabrication due to its lack of necessary controllers. More importantly, using normal-mode AFM would result in the piling up of massive debris, which consists of removed materials, along the fabricated grooves. Considering the existence of such debris, the applied load force $F_z$ can be re-expressed as $F_z = F_{z'} + F_d$, where $F_z$ is the actual load force that contributes to the fabrication depth, and $F_d$ is the machining force caused by the debris. As the applied load force is preset and remains constant during the nanomachining process, the actual load force $F_{z'}$ will decrease, to a greater or lesser degree, and cannot be accurately calculated.

To overcome the disadvantages of normal-mode AFM fabrication, we employed phase-mode AFM for nanomachining along the zigzag and armchair orientations. Unlike the conventional force-mode AFM that achieves controllable nanomachining depths by adjusting the setpoint values, phase-mode AFM is realized by an ultrasonic vibration assisted system, an equivalent point-mass model, and the kinetic energy absorption effect [38, 39]. This allows for directly observing the phase variation and thus detecting the hardness of the fabricated materials. Moreover, the uncontrolled nanomachining depth due to the unavoidable force applied on the debris for normal-mode fabrication will not happen for phase-mode fabrication as the kinetic energy of the loose debris is negligible compared to that of the compact sample consumed. Thus, debris pile-up can be effectively avoided for phase-mode nanomachining.

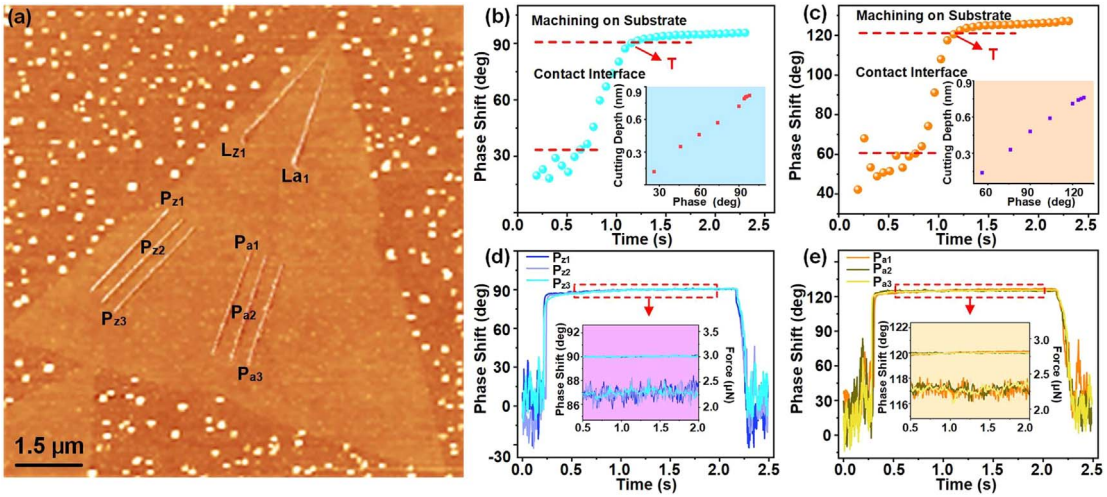


**Figure 5.** Results of phase-mode AFM nanofabrication on monolayer $MoS_2$. (a) is the AFM image showing the experimental results of open-loop and closed-loop fabrication, with $L_{z1}$ and $L_{a2}$ representing the open-loop fabrication paths and $Pz_1$, $Pz_2$, and $Pz_3$, and $Pa_1$, $Pa_2$, and $Pa_3$ the closed-loop fabrication paths. (b) and (c) are the real-time phase shift variations of $L_{z1}$ and $L_{a1}$, respectively. The insets in (b) and (c) are the cutting depth measurements of $L_{z1}$ and $L_{a2}$, respectively. (d) and (e) are the real-time phase shift variations of $Pz_1$, $Pz_2$, and $Pz_3$ and $Pa_1$, $Pa_2$, and $Pa_3$, respectively. The insets in (d) and (e) offer local enlarged views of the phase shift and the corresponding force variation.

The results of phase-mode AFM fabrication, including an open-loop stage ($Lz_1$ and $La_1$) and a closed-loop stage ($Pz_1$, $Pz_2$, and $Pz_3$, and $Pa_1$, $Pa_2$, and $Pa_3$), are shown in figure 5(a). The open-loop stage was executed to obtain the phase variation, from which the specific phase setpoint value that corresponds to the target layers can be obtained and be used as the input for the closed-loop stage fabrication. For the open-loop stage fabrication, the mechanical force applied is linear with the fabrication time. With this linear variation in the force, the phase shift and the corresponding cutting depth for zigzag and armchair orientations were measured and the results are shown in figures 5(b) and (c). It can be seen from phase shift variations that turning points (T) appeared, which was due to the distinctly different hardness between the $MoS_2$ nanosheet and the substrate. Thus, the phase values of the turning points indicated the transition from the $MoS_2$ and the substrate. It should be noted that the specific values of the phase variation for the open-loop and closed-loop stage of the phase-mode fabrication process along the zigzag orientation ($Lz_1$ and $Pz_1$ to $Pz_3$) were different from those of the phase-mode fabrication process along the armchair orientation ($La_1$ and $Pa_1$ to $Pa_3$). Although the specific phase values may vary for the zigzag and armchair fabrication process, the entire phase variation were basically the same and this difference will not affect the force detecting. With the phase values, close-loop fabrication ($Pz_1$, $Pz_2$, and $Pz_3$, and $Pa_1$, $Pa_2$, and $Pa_3$) was conducted, and the corresponding force during nanomachining was detected, which can be used as the necessary load force $F_z$ for evaluating $F_{friction}$. Moreover, from the fabrication results in figure 5(a), it can be seen that the debris was uniformly pushed to both sides of the nanopaths, and the loose packing structure and the negligible hardness of the debris would not affect phase-mode nanomachining. This could help avoid debris pile-up and any force that would otherwise be caused by the debris ($F_d$). From the insets in figures 5(d) and (e), although the detected force fluctuated while fabricating both zigzag and armchair edges, the average value of the force along these two orientations was basically the same, which was approximately 2.3 $\mu$N, and can be regarded as a relatively accurate value for load force $F_z$. After the actual load force $F_z$ was applied, the AFM probe moved on the bare substrate for the same length of 2.5 $\mu$m, and the $F_{friction}$ values along the zigzag and armchair orientations can be obtained by calculating the lateral force, which was approximately 221.7 nN (This value was obtained by eliminating the around 10% increase in friction force amplitude due to the influence of relative humidity [40]). Then, with the appropriate load force applied, normal-mode AFM fabrication was repeated on the $MoS_2$ nanosheet along the zigzag and armchair orientations and the nanomachining force along the zigzag orientation $F_y(\bar{Z})$ and that along the armchair orientation $F_y(\bar{A})$ were calculated to be 237.6 nN and 257.5 nN. By substituting $F_{friction}$, the real cutting forces $F_c$ along the zigzag and armchair lattice orientations were eventually obtained, which were 15.9 nN and 35.8 nN, respectively.

To examine the underlying mechanic mechanism of the nanomachining process, we established a parameterized molecular dynamic MD model to perform simulation. The monolayer $MoS_2$ nanosheets were relaxed in an NVT ensemble, where N represents the total number of system atoms, V the volume, and T the temperature. To sample the physical characteristics of the system, the classical Newton equations of motion were solved numerically using the velocity Verlet algorithm with a time step of 1 fs. Constant NVT MD simulation (a Nose-Hoover thermostat with a temperature of 30 K and a thermostat relaxation time of 0.1 ps)

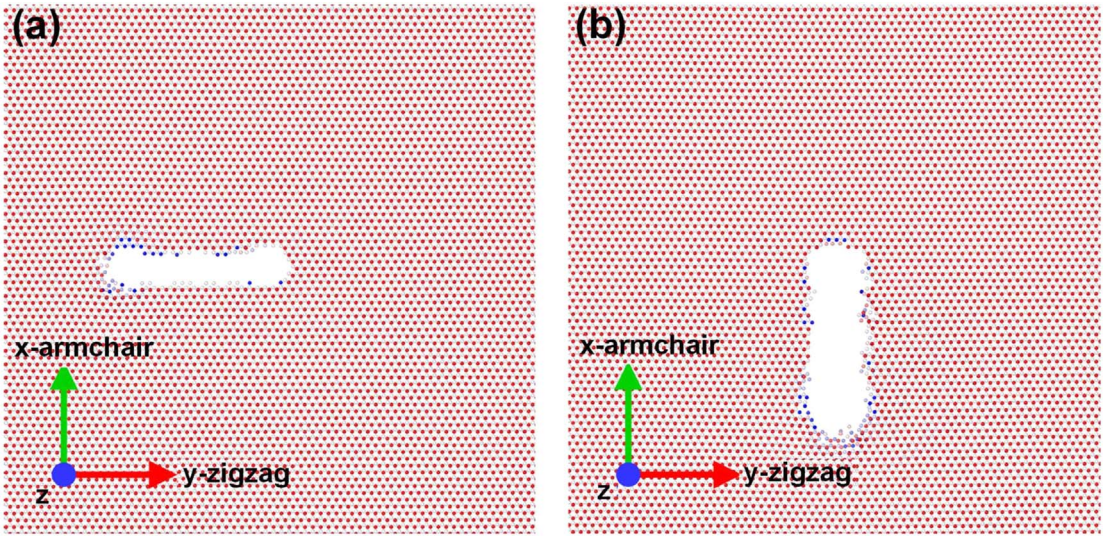


**Figure 6.** Simulation results of nanofabrication on monolayer $MoS_2$. (a) shows the cutting path along the zigzag orientation. (b) shows the cutting path along the armchair orientation.

was performed for 0.1 ns to get equilibrated configuration. Before the simulation, some important parameters should be selected appropriately. As shown in the measurement results (figure S2), the nanoscratch width along the orientation armchair was approximately 1.3 to 1.5 times that along the zigzag orientation. To figure out the reason for this discrepancy, we conducted a systematic review of the available literature. According to the simulation results and detailed analysis in [41] and [42], when a given load force is applied, the fundamental difference in the chirality effect, bonding strength, and edge energy along the zigzag and armchair orientations will lead to a significant difference in the configuration of the initial crack, such as its width, length, and angle. This will in turn result in a significant discrepancy in the crack paths when the crack propagates and extends. As for our experiment, the nanomachining process can be divided into two parts. Firstly, the loading force was generated through the AFM probe and kept in a direction parallel to the zigzag or armchair orientation by rotating the substrate. Due to the chirality effect, two types of initial cracks would be produced as soon as an external load force was applied on the $MoS_2$ nanosheet along the zigzag and armchair orientations. According to a recent MD simulation [43], the armchair orientation comes with higher edge energy than the zigzag orientation, therefore more energy will be released from the initial crack of the former and converted into the motion of adjacent atoms. This suggests that the initial crack along the armchair orientation is wider than that along the zigzag orientation. Secondly, the cutting process on the $MoS_2$ nanosheet was initiated as the AFM probe moved along the initial crack. As the nanomachining continued, the crack discrepancy was aggravated and would eventually result in a huge difference in the nanoscratch width along the two directions. To simulate the nanomachining force with different nanoscratch widths, the parameters should be consistent with the experimental data as much as possible. Considering the enormous computation load, the cutting radii along the two directions were set to 8 Å and 12 Å, respectively, which were proportional to the experimental nanoscratch widths along the zigzag and armchair orientations. Accordingly, the nanomachining speed and length were set to 10 m $s^{-1}$ and 100 Å. A more detailed description on these parameters can be found in Supplementary Information. The simulation results are shown in figures 6(a) and (b). The average force applied to the diamond probe was 12.16 $\pm$ 0.59 nN along the zigzag orientation and 21.45 $\pm$ 0.74 nN along the armchair orientation. More detailed data can be found in Supplementary Information (figure S4).

Based on the simulation results, we managed to theoretically verify the experimentally measured significant discrepancy between the cutting force along the zigzag orientation and that along the armchair orientation. Despite some differences between the experimentally and theoretically measured cutting force values, the cutting force along the armchair orientation is generally larger than that along the zigzag orientation. More specifically, the experimentally obtained cutting force along the armchair orientation is approximately 2.25 times that along the zigzag orientation, whereas the simulated cutting force along the armchair orientation is approximately 1.91 to 1.58 times that along the zigzag orientation. Whether from an experimental or theoretical perspective, the cutting force has a tendency to differ between these two orientations, and the difference in the specific cutting force values can be mainly attributed to different fabrication environments. The nanofabrication by AFM was carried out under ambient conditions, and the process was easily affected by factors such as equipment noise, experimental error, and temperature drift. The simulation, however, was

conducted under ideal conditions, without taking into account these factors that existed for the real experiment. Overall, the experimentally observed discrepancy between the cutting forces along the zigzag and armchair orientations could be theoretically explained by the chirality effect and the crack width difference.

## 4. Conclusions

In summary, the nanofabrication forces along the zigzag and armchair orientations of monolayer $MoS_2$ were demonstrated to be distinctly different by experiment and simulation. The experimental measurements were innovatively performed by combining normal- and phase-mode AFM, showing that the cutting force along the armchair orientation was 35.8 nN, larger than that along the zigzag orientation, which was 15.9 nN. The nanofabrication force discrepancy between these two orientations was further verified by MD simulation ($12.16 \pm 0.59$ nN and $21.45 \pm 0.74$ nN), and the underlying mechanism was attributed to the chirality effect and the crack width difference. Our experimental and theoretical study not only provides a valuable insight into nanofabrication along the zigzag and armchair orientations of monolayer $MoS_2$, but also a promising approach to closed-loop nanomachining on 2D materials along desirable lattice orientations.

## Acknowledgments

This research work was partially supported by the 2019 Science Research Fund Project of Liaoning Provincial Department of Education (Grant Nos. LQGD2019015 and LJGD2019016), China Postdoctoral Science Foundation (Grant Nos. 2019M661124 and 2019M651163), 2020 Liaoning Provincial Natural Science Foundation (2020-BS-144), National Natural Science Foundation of China (Grant Nos. U16132220, 61903359, and 91748212), Scientific Instrument Developing Project of the Chinese Academy of Sciences (Grant No. YJKYYQ20180027) and State Key Laboratory of robotics jointly funded by Liaoning Provincial Department of science and technology (Grant No.2020-KF-22-08).

## ORCID iDs

Meng Li https://orcid.org/0000-0002-2092-939X
Xiaoshi Jin https://orcid.org/0000-0003-0476-7527
Meile Wu https://orcid.org/0000-0002-7055-6958

## References

[1] Carey T, Cacovich S, Divitini G, Ren J, Mansouri A, Kim J M, Wang C, Ducati C, Sordan R and Torrisi F 2017 Fully inkjet-printed two-dimensional material field-effect heterojunctions for wearable and textile electronics *Nat. Commun.* **8** 1–11
[2] Jinzhi L, Min Y, Zhigang S, Shulin M, Xiaojing Z and Yushan X 2012 Experimental study on a designed jet cavitation device for producing two-dimensional nanosheets *Sci. China Technol. Sci.* **55** 2815–9
[3] Vogl T *et al* 2019 Radiation tolerance of two-dimensional material-based devices for space applications *Nat. Commun.* **10** 1–10
[4] Gui G, Li J and Zhong J 2008 Band structure engineering of graphene by strain: first-principles calculations *Phys. Rev. B - Condens. Matter Mater. Phys.* **78** 075435
[5] Dvorak M, Oswald W and Wu Z 2013 Bandgap opening by patterning graphene *Sci. Rep.* **3** 1–7
[6] Gatensby R, Hallam T, Lee K, McEvoy N and Duesberg G S 2016 Investigations of vapour-phase deposited transition metal dichalcogenide films for future electronic applications *Solid. State. Electron.* **125** 39–51
[7] Wang Q H, Kalantar-Zadeh K, Kis A, Coleman J N and Strano M S 2012 Electronics and optoelectronics of two-dimensional transition metal dichalcogenides *Nat. Nanotechnol.* **7** 699–712
[8] Anja F, Sibylle G and Gotthard S 2018 Functional thiols as repair and doping agents of defective $MoS_2$ monolayers *J. Phys. Condens. Matter* **30** 235302
[9] An Y, Hou Y, Gong S, Wu R, Zhao C, Wang T, Jiao Z, Wang H and Liu W 2020 Evaluating the exfoliation of two-dimensional materials with a Green's function surface model *Phys. Rev.* B **101** 075416
[10] An Y, Hou Y, Wang H, Li J, Wu R, Wang T, Da H and Jiao J 2019 Unveiling the electric-current-limiting and photodetection effect in two-dimensional hydrogenated borophene *Phys. Rev. Appl.* **11** 064031
[11] Swain G, Sultana S, Moma J and Parida K 2018 Fabrication of hierarchical two-dimensional $MoS_2$ nanoflowers decorated upon cubic $CaIn_2S_4$ microflowers: facile approach to construct novel metal-free p-n heterojunction semiconductors with superior charge separation efficiency *Inorg. Chem.* **57** 10059–71
[12] Maryam A, Seyedeh Z, Ali R and Seyed M 2018 Sputtered $MoS_2$ layer as a promoter in the growth of $MoS_2$ nanoflakes by TCVD *Mater. Res. Express* **5** 015032
[13] Choi M 2018 Strain-enhanced p doping in monolayer $MoS_2$ *Phys. Rev. Appl.* **9** 024009
[14] Peng K, Zhou J, Gao H, Wang J, Wang H, Su L and Wan P 2020 Emerging one-/two-dimensional heteronanostructure integrating SiC nanowires with $MoS_2$ nanosheets for efficient electrocatalytic hydrogen evolution *ACS Appl. Mater. Interfaces* **12** 19519–29
[15] Liu Y, Li Y, Lu A H, Wang C Q and Ding H R 2017 Mimicking natural paragenetic semiconducting minerals $MoS_2$/sphalerite: a simple method to fabricate visible-light photocatalyst *Sci. China Technol. Sci.* **60** 1870–7

[16] An Y, Hou Y, Wang K, Gong S, Ma C, Zhao C, Wang T, Jiao Z, Wang H and Wu R 2020 Multifunctional lateral transition-metal disulfides heterojunctions *Adv. Funct. Mater.* **30** 2002939
[17] Lei Y, Jiajia Z, Chao F, Guomei X, Chenggen X, Xueqin Y and Bin X 2019 $MoS_2$ nanosheet/$MoS_2$ flake homostructures for efficient electrocatalytic hydrogen evolution *Mater. Res. Express* **6** 085005
[18] Zhang X J, Chen K Q, Tang L M and Long M Q 2011 Electronic transport properties on V-shaped-notched zigzag graphene nanoribbons junctions *Phys. Lett. Sect. A Gen. At. Solid State Phys.* **375** 3319–24
[19] Chen Q, Li H, Xu W, Wang S, Sawada H, Allen C S, Kirkland A I, Grossman J C and Warner J H 2017 Atomically flat zigzag edges in monolayer $MoS_2$ by thermal annealing *Nano Lett.* **17** 5502–7
[20] Dolui K, Pemmaraju C D and Sanvito S 2012 Electric field effects on armchair $MoS_2$ nanoribbons *ACS Nano* **6** 4823–34
[21] Ouyang F, Yang Z, Ni X, Wu N, Chen Y and Xiong X 2014 Hydrogenation-induced edge magnetization in armchair $MoS_2$ nanoribbon and electric field effects *Appl. Phys. Lett.* **104** 071901
[22] Gut D, Prokop M, Sticlet D and Nowak M P 2019 Valley polarized current and resonant electronic transport in a non-uniform $MoS_2$ zigzag nanoribbon *Phys. Rev.* B **101** 08542
[23] Li X, Zhao K, Zhang L, Ding Z and Hu K 2017 $MoS_2$-decorated coaxial nanocable carbon aerogel composites as cathode materials for high performance lithium-sulfur batteries *J. Alloys Compd.* **692** 40–8
[24] Qi J, Lan Y W, Stieg A Z, Chen J H, Zhong Y L, Li L J, Chen C D, Zhang Y and Wang K L 2015 Piezoelectric effect in chemical vapour deposition-grown atomic-monolayer triangular molybdenum disulfide piezotronics *Nat. Commun.* **6** 1–8
[25] Qu Y, Shili C and Jun K 2012 Bandgap tuning in armchair $MoS_2$ nanoribbon *J. Phys :Condens Matter Mater* **24** 335501
[26] Zhang L, Wan L, Yu Y, Wang B, Xu F, Wei Y and Zhao Y 2015 Modulation of electronic structure of armchair $MoS_2$ nanoribbon *J. Phys. Chem.* C **119** 22164–71
[27] Tiwari D L and Sivasankaran K 2020 NDR behavior of a phosphorous-doped double-gate $MoS_2$ armchair nanoribbon field effect transistor *J. Electron. Mater.* **49** 551–8
[28] Ke X, Bittencourt C and van Tendeloo G 2015 Possibilities and limitations of advanced transmission electron microscopy for carbon-based nanomaterials *Beilstein J. Nanotechnol.* **6** 1541–57
[29] Paillet M, Parret R, Sauvajol J-L and Colomban P 2018 Graphene and related 2D materials: an overview of the Raman studies: graphene and related 2D materials *J. Raman Spectrosc.* **49** 8–12
[30] Li H, Zhang Q, Yap C C R, Tay B K, Edwin T H T, Olivier A and Baillargeat D 2012 From bulk to monolayer $MoS_2$: evolution of Raman scattering *Adv. Funct. Mater.* **22** 1385–90
[31] Van Der Zande A M, Huang P Y, Chenet D A, Berkelbach T C, You Y, Lee G H, Heinz T F, Reichman D R, Muller D A and Hone J C 2013 Grains and grain boundaries in highly crystalline monolayer molybdenum disulphide *Nat. Mater.* **12** 554–61
[32] Li M, Zhang Y, Yu P, Xi N, Wang Y and Liu L 2017 A novel and facile method for detecting the lattice orientation of $MoS_2$ tribological surface using the SPSA process *Mater. Des.* **135** 291–9
[33] Li M, Shi J, Xi N, Wang Y and Liu L 2018 Layer-controllable nanofabrication of two-dimensional materials with phase-mode AFM *Mater. Lett.* **232** 43–6
[34] Wang Y, Zhang K and Xie G 2016 Remarkable suppression of thermal conductivity by point defects in $MoS_2$ nanoribbons *Appl. Surf. Sci.* **360** 107–12
[35] Jiang J W, Park H S and Rabczuk T 2013 Molecular dynamics simulations of single-layer molybdenum disulphide ($MoS_2$): Stillinger-Weber parametrization, mechanical properties, and thermal conductivity *J. Appl. Phys.* **114** 064307
[36] Jiang Jin-Wu 2015 Parametrization of Stillinger-Weber Potential Based on Valence Force Field Model: Application to Single-Layer MoS2 and Black Phosphorus *Nanotechnology* **26** 315706
[37] Xie H, Vitard J, Haliyo S, Régnier S and Boukallel M 2008 Calibration of lateral force measurements in atomic force microscopy with a piezoresistive force sensor *view of Scientific Instruments* **79** 033708
[38] Shi J, Liu L, Yu P and Li G 2017 Phase mode nanomachining on ultra-thin films with atomic force microscopy *Mater. Lett.* **209** 437–40
[39] Shi J, Liu L and Li G 2016 The co-design of interface sensing and tailoring of ultra-thin film with ultrasonic vibration-assisted AFM system *Nanotechnology* **27** 235302
[40] Zhao X and Perry S S 2010 The role of water in modifying friction within $MoS_2$ sliding interfaces *ACS Appl. Mater. Interfaces* **2** 1444–8
[41] Bao H, Huang Y, Yang Z, Sun Y, Bai Y, Miao Y, Chu P K, Xu K and Ma F 2018 Molecular dynamics simulation of nanocrack propagation in single-layer $MoS_2$ nanosheets *J. Phys. Chem.* C **122** 1351–60
[42] Baoming W, Zahabul I, Kehao Z, Ke W, Joshua R and Aman H 2017 Role of sulphur atoms on stress relaxation and crack propagation in monolayer $MoS_2$ *Nanotechnology* **28** 365703
[43] Wu J, Cao P, Zhang Z, Ning F, Zheng S S, He J and Zhang Z 2018 grain-size-controlled mechanical properties of polycrystalline monolayer $MoS_2$ *Nano Lett.* **18** 1543–52